

Optical and Raman spectroscopies of $^{171}\text{Yb}^{3+}:\text{Y}_2\text{SiO}_5$ hyperfine structure for application toward microwave-to-optical transducer

Hee-Jin Lim,* Gahyun Choi, and KeeSuk Hong

Korea research institute of standards and science (KRISS), Daejeon 34113, Korea

Abstract

This study analyzed the optical techniques for high resolution, low-noise spectroscopy of a hyperfine structure (HFS) made of ytterbium-isotope 171 ions ($^{171}\text{Yb}^{3+}:\text{Y}_2\text{SiO}_5$). Large energy spacings in $^{171}\text{Yb}^{3+}$ are advantageous for spin-state preparations of quantum memory and construction of a transducer, thereby promoting the simultaneous stable control of the optical frequencies of lasers over a wide range of 3 GHz. We also built our own 2.7-K cryogenic system for optical, radio-wave-assisted spectroscopy. We attained to high resolution and sensitivity both in pump-probe saturation spectroscopy (PPS) and Raman heterodyne spectroscopy (RHS). Our frequency-stabilized PPS achieved a high-resolution spectrum of the HFS, whereas our setup of RHS enabled the efficient detection of paramagnetic spin resonance efficiently for a wide range of radio frequencies. As the underlying Raman process is an up-converting transduction, we present the optimization of the sensitivity of Raman heterodyne detections by selecting the best crystal orientation and efficient radio-wave coupling in future applications toward photon transducers.

Keywords: Ytterbium ion, Spin ensemble, Raman heterodyne spectroscopy, Hyperfine structure, Paramagnetic spin resonance

*Electronic address: heejin.lim@kriss.re.kr

I. INTRODUCTION

Spin ensembles of rare earth ion (RE^{3+}) [1, 2] in optical crystals have been actively studied as materials for application in quantum memory [3, 4] with long coherence storage time [5] and in photon transducers [6, 7]. This material features coherent interactions both with optical [8] and microwave photons [9, 10]. Coherence transfers between spins [11] and between optical photons and nuclear spins [12], which are crucial in the access protocol of quantum memory, have been demonstrated with the material.

Raman heterodyne spectroscopy, which exploits coherence transfer from a spin transition to an optical transition, has been widely used for reading coherent spins [5], enabling the optical observation of spin transient oscillations.[13, 14] Recently, complementary methods of using nano-photonics [15, 16] and microwave resonators in addition to optical resonators [15, 17, 18] were proposed to enhance the efficiency of such coherent up-conversion process. However, one important task is still remained for high-efficiency, high-fidelity state preparation.[19] The preparation of optical methods in the case of spin-ensemble quantum memory, comprising of complete depletion of both target states and a optical frequency domain for address and followed by re-pumping the nuclear spin states back to the optical domain with addressed frequencies, can be limited for fine manipulations in some RE^{3+} 's of dense spin structures, due to large optical inhomogeneous broadening that commonly exists for RE^{3+} doped in solid crystals.[20, 21]

Among the many known RE^{3+} , ytterbium-isotope-171 ion doped in yttrium orthosilicate ($^{171}\text{Yb}^{3+}:\text{Y}_2\text{SiO}_5$) has been expected to overcome the limitation.[22] $^{171}\text{Yb}^{3+}$ has a simple hyperfine structure (HFS) owing to a small quantum number of nuclear spin ($I = 1/2$), and also large energy spacing from hundreds of megahertz (MHz) to a few gigahertz (GHz).[23, 24] Its HFS is widely ranged over 3 GHz in optical frequency, as reported in this article. Despite such a wide range, stability and precision of frequency are still required for addressing the spin state in quantum memory applications. In the case of $^{171}\text{Yb}^{3+}:\text{Y}_2\text{SiO}_5$, we must determine how to control the optical frequencies of lasers with high precision or high repeatability. In addition, a method must be devised to achieve good stability with free or dynamic selection in wide ranges.

This study presents a control system for optical frequencies. The system was applied to precise spectroscopies for $^{171}\text{Yb}^{3+}$ with a laboratory-designed low-temperature setup. Our

system can simultaneously control two lasers, and maintains their optical frequencies locked using high speed feedbacks to a cavity reference and a radio-frequency (RF) source.

We performed two spectroscopies, namely, pump-probe saturation spectroscopy and Raman heterodyne spectroscopy.[13] These two spectroscopies were done in 2.7 kelvins (K), where long coherence time (T_2) is allowed for various quantum memory experiments.[25, 26] Using pump-probe saturation spectroscopy, we achieved high-resolution and high-sensitivity spectra of the $^{171}\text{Yb}^{3+}$ HFS. The results of the hyperfine resolution are discussed in Section III.

Using a cryostat designed both for Raman heterodyne spectroscopy and vibration isolations, we succeeded in directly detecting spin resonance using the optical method. We optimized the intensity of the Raman heterodyne signals using a crystal orientation to maximize the coupling strength between radio-waves and spin transitions based on efficient feed-line circuits for the radio-waves. We devised an impedance-matched coplanar waveguide on a copper printed-circuit-board, which could be easily replaced with a superconducting resonator [18] in future works to challenge the high-efficiency of photon transduction. The results of the instrumental optimization of sensitivity are discussed in Section IV.

II. SPECTROSCOPY APPARATUS AND METHODS

A. Low-temperature setup for Raman heterodyne spectroscopy

Raman heterodyne spectroscopy is an optical method used to detect the spin resonance of radio-waves.[13, 14] This method requires the collection of heterodyne beats between the optical pump and the Raman waves. In particular, the generation of Raman waves can be enhanced by the spin resonance of radio waves (transition of $S_1 \rightarrow S_2$) within a cyclic process completed by an optical pump ($S_2 \rightarrow E_x$) and an emission of Raman waves ($E_x \rightarrow S_1$), as shown in the inset of Figure 1(a). In this process, the enhanced heterodyne beat should have the same frequency as that of the spin transition. Our simple setup for the heterodyne detection is depicted in Figure 1(a), where detection can be minimally performed using a vector network analyzer (VNA) and a fast photodiode of 10-GHz bandwidth. VNA is a useful tool for generating and receiving radio waves, producing a spectrum of the transmission S-parameter (S_{21}) of the generated frequency of radio waves (Ω).

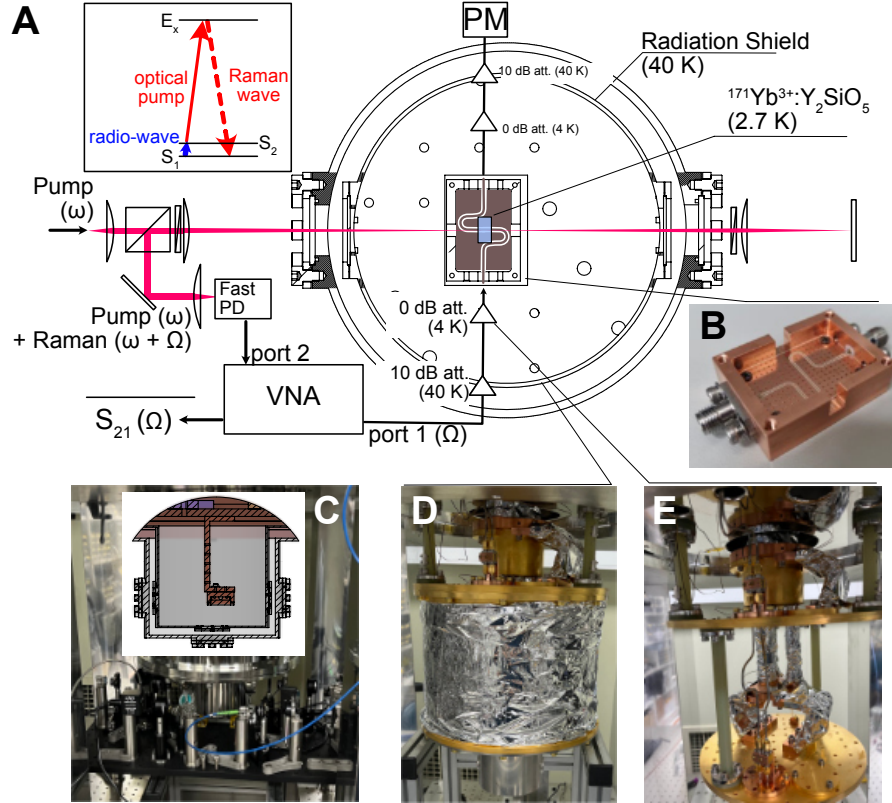


FIG. 1: (Color online) Experimental setup for low-temperature Raman heterodyne measurements. (a) Schematic of the setup for optical- and radio-frequency interactions of $^{171}\text{Yb}^{3+}:\text{Y}_2\text{SiO}_5$ in refrigeration. (b) Microwave coplanar waveguide in a copper box for feeding a radio-waves in $^{171}\text{Yb}^{3+}:\text{Y}_2\text{SiO}_5$. (c,d) Thermal-radiation-shield apparatus for optical experiments. (e) Thermally protected radio-frequency feed lines.

However, refrigeration to below 4 K is required to ease the rate of spin relaxation (T_1^{-1}) toward the thermal equilibrium population of S_1 and S_2 . The main source of relaxation in spin ensembles of rare ion (RE^{3+}) in Y_2SiO_5 are the phonon interactions [1], which display a more intensive impact through two phonon processes at higher temperatures.[27] Studies have shown that the spin relaxation rate of $^{171}\text{Yb}^{3+}:\text{Y}_2\text{SiO}_5$ can be lower than 10 Hz at < 4 K.[28] Therefore, our setup was devised to refrigerate Y_2SiO_5 to < 2.7 K by using a pulse tube cryocooler (Cryomech PT405). Figure 1(c-e) shows the internal structures of our designed cryostat. To isolate thermal radiation through optical windows, we installed cold windows at the 30-K radiation shield. In addition, we used semi-rigid coaxial cables made of stainless steel to deliver a high-frequency radio waves to $^{171}\text{Yb}^{3+}:\text{Y}_2\text{SiO}_5$. Furthermore, low-

stiffness copper braids wound with multilayer insulation films were used to isolate vibrations while allowing a large cooling capacity.

For an efficient RF coupling with respect to $^{171}\text{Yb}^{3+}$, we installed a cube of $^{171}\text{Yb}^{3+}:\text{Y}_2\text{SiO}_5$ crystal on a printed circuit board, in which a microwave coplanar waveguide with a matched characteristic impedance was inscribed. This radio-wave setup is protected from electromagnetic noises by using a copper box, as shown in Figure 1(b).

As the RF magnetic field is formed locally around the central conductor of the coplanar waveguide,[29] the Raman generations enhanced by resonant radio waves can occur for the $^{171}\text{Yb}^{3+}$ that locates near this conductor. Therefore, the optimizations involves an increase in the optical power density in this region until photocurrents and electrical amplification in the fast photodiode do not saturate. In our setup, the pump laser beam of 1-mW power was focused toward an area of ~ 0.1 -mm diameter with slow beam divergence, located near the central conductor, and adjusted to avoid surface scattering. We ensured that the beam direction was parallel to the waveguide direction to achieve maximum overlap between the optical path and the RF magnetic field. The Y_2SiO_5 crystal was carefully oriented on the waveguide such that the crystallographic b -axis was aligned perpendicular to the waveguide direction. This crystal orientation allows the maximization of the coupling strength between the radio waves and spin transitions, benefited by anisotropy of magnetic susceptibility. The theoretical discussion is detailed in Section IV.

For our sample, we ordered to substitute 50 ppm of crystallographic yttrium sites (site I and site II) with isotopically purified $^{171}\text{Yb}^{3+}$. Considering that the two crystallographic sites in Y_2SiO_5 have different optical transition frequencies and HFSs, the population in the interaction should be counted only for a specific site. The total population excited by the pump laser is approximately 3.8×10^{13} for the length of the optical path inside Y_2SiO_5 used in this study (10 mm).

B. Optical frequency control system

The stabilization of a relative optical frequency between the pump (master) and probe (slave) lasers enables highly sensitive and repeatable detections, thus allowing high precision when resolving the HFS of $^{171}\text{Yb}^{3+}:\text{Y}_2\text{SiO}_5$. In addition, the stabilization of the master laser and the relative frequency of the slave laser allows spin-state addressing with absolute optical

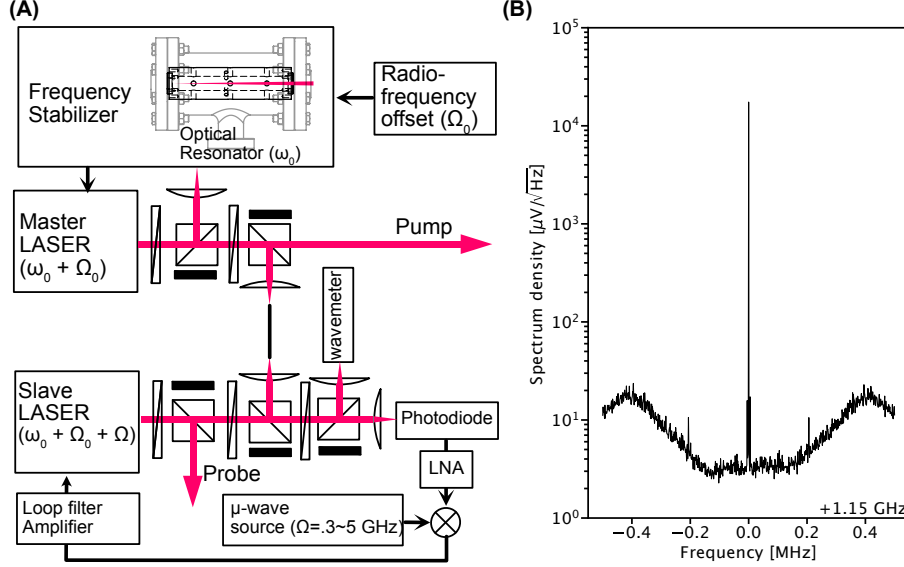


FIG. 2: (a) Laser-frequency stabilizing system. (b) Beat spectrum of interference signals between the master and the slave lasers. The horizontal axis represents the beat frequency relative to 1.15 GHz, which corresponds to the difference in the optical frequencies of the lasers. The spectrum for the main 1.15-GHz signal is detailed as a phase noise chart in the supplementary materials.

frequencies for future quantum memory applications. Our dual schemes of stabilization also provide protection from environmental acoustic noises at higher levels.

Our system for optical frequency control for pump and probe lasers combines the optical cavity lock [30] and optical phase lock loop techniques(OPLL) [31]. For an optical cavity reference, we adopted the electronic side-band (ESB) modulation technique [30], as depicted by the the frequency stabilizer box in Figure 2(a). This method has a lock point offset by a radio-frequency (Ω_0) from the cavity resonance (ω_0). Therefore, we could maintain the stability of the master laser at the desired frequency. Details of our ESB method are explained in the supplementary materials. In this study, we constructed an ultra-high-vacuum body for an optical cavity with high reflectivity ($> 99.9\%$ concave mirrors) and achieved a low error density $< 10 \text{ Hz}/\text{Hz}^{1/2}$ for the locked optical frequency within the measurement bandwidth of 10 kHz, using a commercial fast PID controller (Toptica FALC pro).

The phase detection of the slave laser in our OPLL setup was processed through generating optical beats and comparing their phase with a radio-frequency (Ω) reference, as shown in Figure 2(a). The electronic signals for the optical beat were generated from an

impedance-matched photodiode of 10-GHz bandwidth and were amplified using a low-noise amplifier (LNA). The down-conversion of the beat frequency with a mixer driven by the local oscillator (LO) frequency (Ω) plays the role of a phase detector, and the converted signal modulates the electric currents for the slave laser through the filter amplifiers of the PID controller. We employed external cavity diode lasers (ECDL) for both master and slave lasers, taking advantages of the high-speed frequency response (< 200 MHz) to electric currents. Stable phase conditions in the feedback loop were observed for a beat frequency identical to the LO frequency, to allow the tuning of the lock point of relative frequency by adjusting the LO frequency. Therefore, the locked frequency of the slave laser was determined by Ω . In addition, we achieved a wide tuning range from 300 MHz to 3 GHz, and a continuous sweep range of 100 MHz. The second range was limited by a radio-wave synthesizer (because of sweep discontinuity of fractional PLL and internal switches).

The spectrum of optical beats locked at 1.15 GHz (Figure 2(b)) showed a high level of noise suppression and frequency accuracy. Although this feedback loop was designed to consider low-phase noise, we optimally tuned it for frequency sweep at the expense of phase noise reduction, still confirming a frequency error far smaller than 1 kHz. Note that all frequency synthesizers and receivers, including spectrum analyzer, were synchronized according to the Rubidium frequency standard (SRS FS725).

III. HYPERFINE STRUCTURE

$^{171}\text{Yb}^{3+}$ demonstrates nuclear spin with a quantum number of $I = 1/2$, thus displaying a HFS in both the lowest-lying crystal-field (CF) state $^2\text{F}_{7/2}(0)$ and in the optically accessible CF state $^2\text{F}_{5/2}(0)$ as shown by the energy diagram in Figure 4(d). The strong coupling strength between the electron and nuclear spins causes large energy splittings in the HFS of $^2\text{F}_{7/2}(0)$. The eigen-states of $^2\text{F}_{7/2}(0)$ are denoted as $A_{1,2}$ and $B_{1,2}$ and those of $^2\text{F}_{5/2}(0)$ are denoted by $C_{1,2,3,4}$. The representation of the eigen-states with electron (\uparrow, \downarrow) and nuclear spins (\uparrow, \downarrow), as shown in Figure 4(d), depends on the setting of the quantization axis, and can slightly differ from those presented in earlier studies [24, 32].

Using our frequency control system with a long tuning range and excellent stabilization performance, we could measure a highly accurate HFS spectrum at 2.7 K, as shown as Figure 3. To increase sensitivity, we adopted the frequency modulation (FM) technique

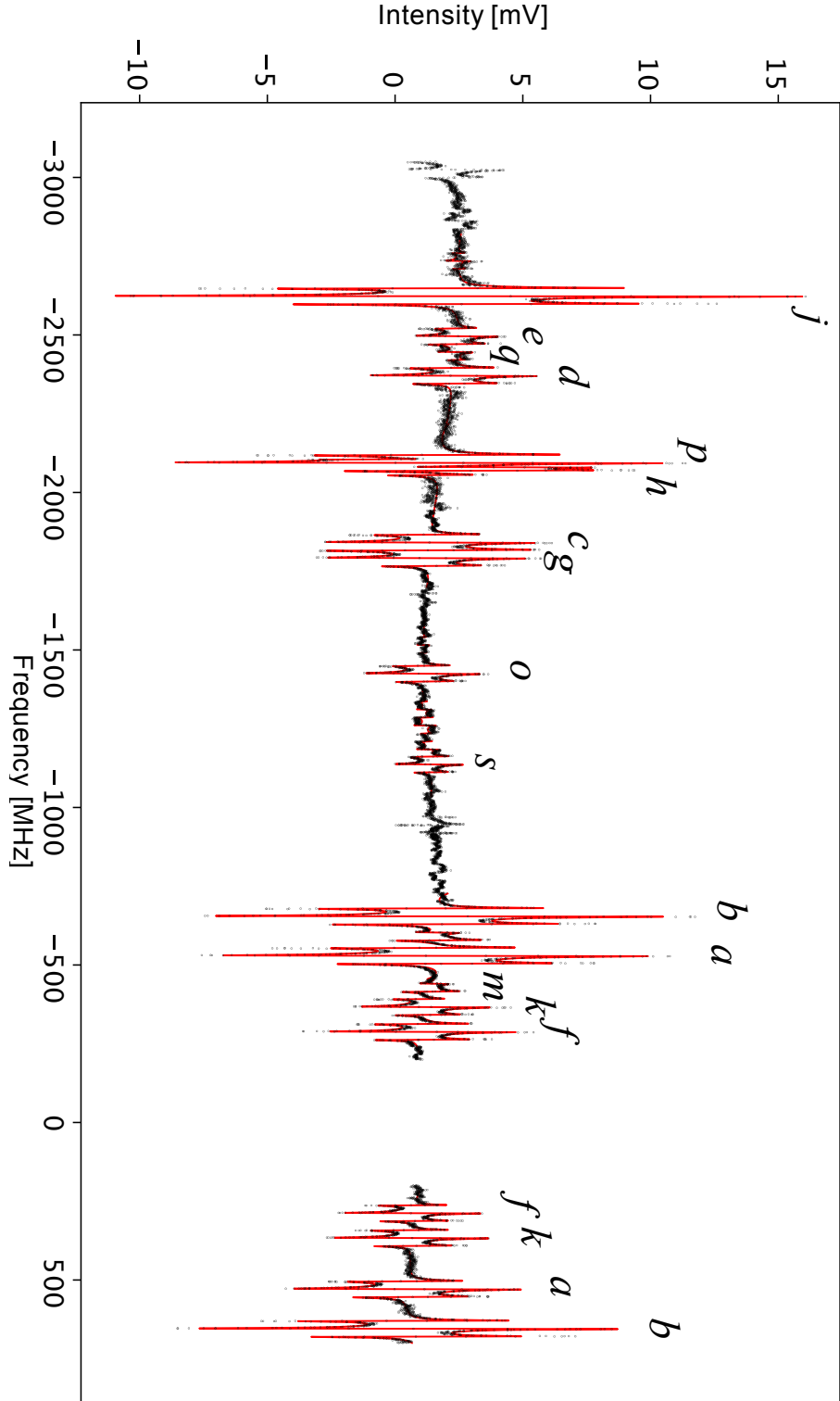


FIG. 3: Pump-probe saturation spectrum of $^{171}\text{Yb}^{3+}:\text{Y}_2\text{SiO}_5$ (crystallographic site II) at 2.7 K. The horizontal axis represents the optical frequency difference between the pump and probe lasers. Resonances are represented by small letters (a - s).

using a phase-modulating electro-optic modulator.[33] The counter-propagating pump and probe beams were laid on the same path and at the same linear polarization in the plane of $D_1 - D_2$ axes of Y_2SiO_5 . Because they are distinguished only by their propagating directions, we devised to identify them using a circulator setup of comprising a Faraday rotator and a calcite polarizer. This setup could choose a polarization to obtain the maximum optical absorption. The power of the pump (probe) was 10 (0.1) mW within area of a 1-mm beam diameter.

As shown in Figure 3, pump-probe spectroscopy displayed many resonance signals within the spectrum. The pump frequency for $^{171}Yb^{3+}$ at crystal site II of yttrium in Y_2SiO_5 was selected as 306.2685 THz, excited simultaneously from $\{A_1, A_2\}$ to $\{C_3, C_4\}$ and from $\{B_1, B_2\}$ to C_2 to recirculate spin state populations. The horizontal axis of the spectrum displays the relative frequency of the probe laser to the pump laser. The values of the half-width-half-maximum linewidth were measured between 1 and 1.5 MHz. The linewidths were attributed to inhomogeneous broadening inside $^2F_{7/2}(0)$ and inside $^2F_{5/2}(0)$, affected by a mechanical strain in Y_2SiO_5 . [24, 28] (Details about the resonance frequency and linewidth are provided in supplementary materials.)

The physical origins of resonances (a - s) observed in the spectrum in Figure 3 can be explained with the energy diagrams shown in Figure 4(a-c). The transitions resonant with pump and probe lasers of configurations a - e share the same optically excited state. Therefore, the spectrum positions of a - e are coincident with the energy spacing of the $^2F_{7/2}(0)$ spin eigen-states. From the spectrum positions of f - j , we extracted the energy spacings for $^2F_{5/2}(0)$.

However, resonances of k - s are complicated, because the transitions interacting with the pump and probe lasers have no common state, as shown as Figure 4(c). They exhibited smaller signal intensities, enabled by additional processes of relaxations intermediate between the pump and probe transitions. Their spectral positions were matched with algebraic relations of energy spacing, as noted in a supplementary table (supplementary materials). As observed, the blank spaces denote resonances that were weakly detected.

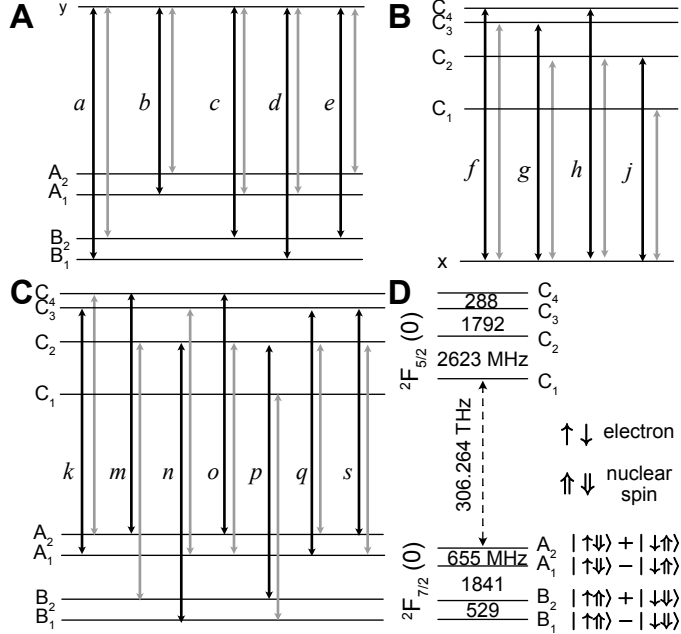


FIG. 4: Hyperfine structure of $^{171}\text{Yb}^{3+}:\text{Y}_2\text{SiO}_5$ as the origin of pump-probe resonance. (a-c) The origin of resonance signals appearing in Figure 3. Black (gray) arrows indicate transitions interacting with the pump (probe) laser. (d) Hyperfine structure of the lowest-lying crystal field (CF) state ${}^2F_{7/2}(0)$ and the optically accessible ${}^2F_{5/2}(0)$ for $^{171}\text{Yb}^{3+}$ at crystallographic yttrium site II of Y_2SiO_5 .

IV. EXPERIMENTAL RESULTS OF RAMAN HETERODYNE SPECTROSCOPY

The main results of Raman heterodyne measurements are displayed by the spectrum in Figure 5(a). In this spectrum, radio-wave resonance were observed for spin transitions of $A_1 \leftrightarrow A_2$, $B_1 \leftrightarrow B_2$, and $A_2 \leftrightarrow B_2$, denoted as $T(a)$, $T(b)$, and $T(ab)$ respectively as in the energy diagram of Figure 5(b). Furthermore, we observed that the resonant frequencies and linewidth of the radio-waves were identical to those obtained by the pump-probe saturation spectroscopy.

The signal intensity depends on the magnetic susceptibility of the transition and the optical frequencies of the pump laser. Here, we set the optical frequency of pump laser close to the transition energy of $A_2 \leftrightarrow C_1$, but slightly offset it by 1.5 GHz. This offset is similar to a full-width-half-maximum width of optical inhomogeneous broadening, and could maximize for maximizing the $T(a)$ signal intensity by avoiding the depletion of $\{A_1, A_2\}$. Then, the $T(a)$ signal intensity includes a contribution from the process comprising of a radio-wave

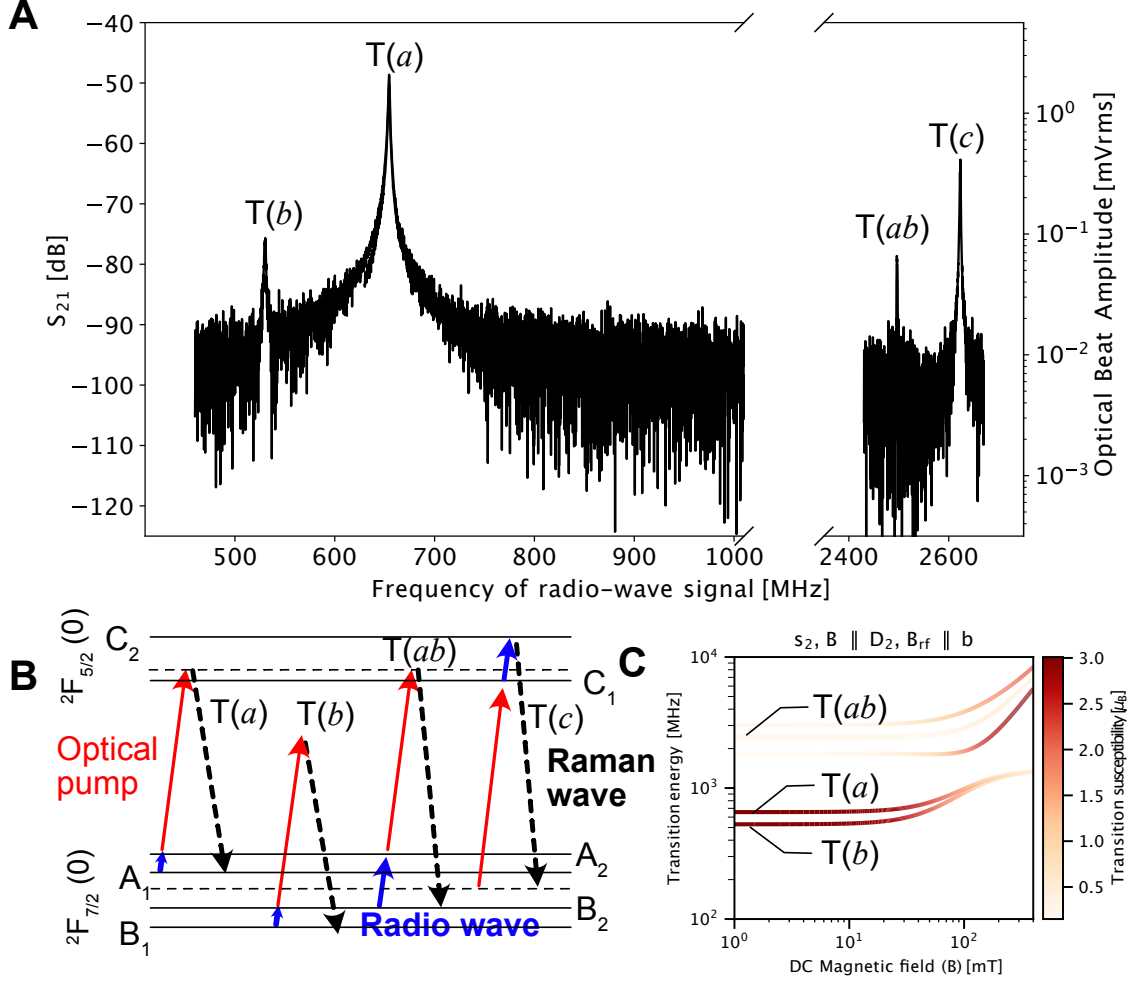


FIG. 5: Raman heterodyne spectra of $^{171}\text{Yb}^{3+}:\text{Y}_2\text{SiO}_5$ - site II spin resonance. **(a)** Horizontal axis denotes the radio-wave frequency. S_{21} denotes the logarithm ratio of the power of a Raman heterodyne beat to the power of radio waves fed into the copper box. RF power is -12 dBm ($63 \mu\text{W}$), and the optical power is 1.3 mW with a 0.1-mm diameter. **(b)** Energy diagram of the observed spin resonances of Raman heterodyne process. **(c)** Spin energies calculated using the spin Hamiltonian of $^2F_{7/2}(0)$. The color displays the transition magnetic susceptibility normalized by the Bohr magneton, implying the coupling strength of the radio-wave.

driving $A_2 \leftrightarrow A_1$, optical pump $A_1 \rightarrow C_1$, and Raman wave generation $C_1 \rightarrow A_2$, as well as the configuration $\{A_1 \rightarrow A_2, A_2 \rightarrow C_1, C_1 \rightarrow A_1\}$ presented in Figure 5(b). Although the pump laser frequency became close to the $B_2 \rightarrow C_1$ excitation by the offset, the optical pumping seems still selective in the excite $\{A_1, A_2\}$ than $\{B_1, B_2\}$. From a study of optical absorption spectrum (supplementary materials), $\{B_1, B_2\}$ prefers optical excitations into

$\{C_2, C_3, C_4\}$ than into C_1 , which may depend on our setting of polarizations, or sample characteristics. In this case, Raman heterodyne detections for $\{B_1, B_2\}$ states requires > 3 -GHz greater optical frequencies of the pump to be excited to $\{C_2, C_3, C_4\}$.

The weak signal intensity of T(c) is due to a negligibly small magnetic susceptibility of transition, as shown as Figure 5(c). To theoretically achieve this value of transition strength, we first calculated the spin-state spacing and its eigen-state from the spin Hamiltonian (\hat{H}) of electron and nuclear spins (\hat{S}, \hat{I}) using a symmetric hyperfine tensor A_{ij} , symmetric gyromagnetic tensor g_{ij} for $i, j \in \{D_1, D_2, b\}$, Bohr magnetron μ_B , and magnetic field B [22–24]:

$$\hat{H} = \mu_B g_{ij} B_i \hat{S}_j + A_{ij} \hat{S}_i \hat{I}_j. \quad (1)$$

With spin eigen-states of $\psi_\alpha \in \{A_1, A_2, B_1, B_2\}$, the transition magnetic susceptibility ($\vec{\chi}$) can be defined as

$$\vec{\chi}_{\alpha\beta} = \mu_B \left\langle \psi_\alpha \left| \vec{g} \cdot \hat{S} - \frac{\vec{B}_{\text{DC}}(\vec{B}_{\text{DC}} \cdot \vec{g} \cdot \hat{S})}{|\vec{B}_{\text{DC}}|^2} \right| \psi_\beta \right\rangle. \quad (2)$$

Here, subtraction can correct the transition strength, keeping only the oscillation component of the magnetic dipole induced by a radio-wave magnetic field (\vec{B}_{rf}), excluding the DC magnetization component generated by strong magnetic fields (\vec{B}_{DC}).[28] The g_{ij} of $^{171}\text{Yb}^{3+}:\text{Y}_2\text{SiO}_5$ displays large anisotropy, such that it increases to ~ 6 for a \vec{B} direction close to b -axis of Y_2SiO_5 , but it can be diminished to < 1 for the other directions.[23]

By taking advantages of the g_{ij} anisotropy to obtain a large interaction strength between radio-waves and resonant spin transitions, we aligned the b -axis parallel to \vec{B}_{rf} of the coplanar waveguide mode. We expected a high value of $\chi \sim 3\mu_B$ for $A_1 \leftrightarrow A_2$ and $B_1 \leftrightarrow B_2$ even though they exist in the electron-nuclear mixture under low $B_{\text{DC}} < 20$ mT, as shown as Figure 5(c). In this calculation, χ of the transition $A_2 \leftrightarrow B_2$ of T(ab) was a small value.

Because of the efficient radio-wave coupling effect and optical beat detection, the radio-wave power set for obtaining the spectrum (Figure 5) was -12 dBm (63 μW) corresponding to 0.08 mT of peak RF magnetic field strength. Note that this was achieved without the use of an RF amplifier. The absolute optical power of the generated Raman for T(a) was 2 nW, which was converted from the optical beat amplitude (2 mV_{rms}) using the RF conversion gain of the photodiode (1200 V/W) and the power of optical LO (1.5 mW). As we did not use an RF resonator, most of the power of the radio-waves passed though the waveguide,

and the probability of resonant scattering and absorption of radio-wave photons are very low in this configuration. Therefore, applying a definition of the conversion efficiency as a Raman photon rate over the driving RF photon flux rate seems early for consideration. Nevertheless, this paper presents the outcome of crude estimation as 7×10^{-11} ($= 2 \text{ nW} / 306 \text{ THz} \times 655 \text{ MHz} / 63 \text{ } \mu\text{W}$).

Here, $T(c)$ is unexpected because it originates in the transition $C_1 \leftrightarrow C_2$. Note that we did not theoretically study χ for the transition inside ${}^2F_{5/2}(0)$ because of lack of information. That is also because decisive factors, such as g_{ij} and A_{ij} , were studied mainly for the lowest-lying CF state (${}^2F_{7/2}(0)$) by using electron-paramagnetic resonance measurements. Herein, we report that transition $C_1 \leftrightarrow C_2$ displays high χ , and spin states in ${}^2F_{5/2}(0)$ can be termed as valuable subjects of optically accessible spin ensembles.

V. CONCLUSIONS

The high-resolution and low-noise spectra derived using the proposed system represent reliable noise rejection performance through feedback controls for generating optical and radio-wave frequencies. Using the proposed system, the HFS and spin resonances of ${}^{171}\text{Yb}^{3+}:\text{Y}_2\text{SiO}_5$ could be measured accurately. Techniques that we employed to obtain the sensitive spectrum of HFS are suitable for the frequency reference in the precise quantum memory experiment with ${}^{171}\text{Yb}^{3+}$ in near future. The spectroscopy methods developed in this study could facilitate in the control, measurement, and preparation of ${}^{171}\text{Yb}^{3+}$ spin states required by quantum memory and transducer applications.

The importance of selecting the pump frequency related with the depletion phenomenon were observed in this study. Figure 6 shows the effect of the phenomenon on Raman heterodyne signals through the suppression of the $T(a)$ signal. This could be achieved when the optical pump frequency is resonant with $\{A_1, A_2\} \leftrightarrow C_1$ and in a stable lock condition. This result can be attributed to the optical pump, $\{A_1, A_2\} \rightarrow C_1$, moving populations toward $\{B_1, B_2\}$. Our next study will be constructing a strong spin polarization between A_1 and A_2 . This is challenging because its transition energy is low to resist forces toward thermal equilibrium at 2.7 K, and the spin states rarely avoid spectral mixing in the optical domain owing to inhomogeneous broadening between ${}^2F_{7/2}(0)$ and ${}^2F_{5/2}(0)$. Nevertheless, as we observed the strong state depletion, we expect to find some clues from our radio-wave

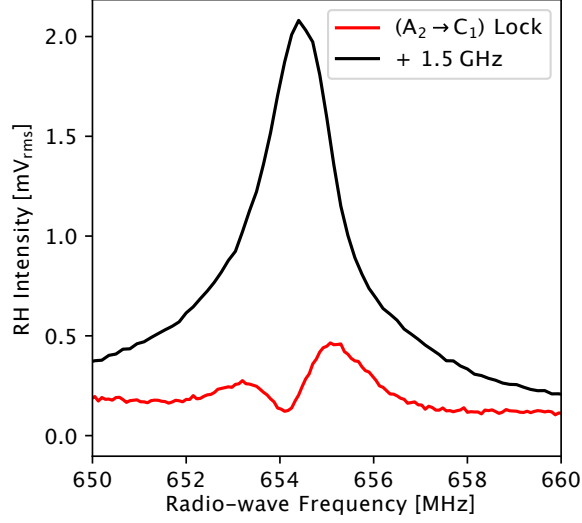


FIG. 6: Effects of optical pump frequency and its stability on Raman heterodyne signal. The red curve was obtained with the resonant optical frequency under lock condition. The black curve represents the Raman heterodyne spectrum for a 1.5-GHz detuned optical pump.

assisted optical spectroscopy; future protocols of state preparation may be devised using resonant radio waves assisted by optical transitions optimally addressed by optical pumping. The addressing method will be processed by a complete depletion of both $\{A_1, A_2\}$ and address domain and followed by a sharp addressing pump from $\{B_1, B_2\}$ through $\{C_3, C_4\}$, whose relative frequencies of pump lasers are +0 GHz (306.264 THz) with a sweep width of 200 MHz for depletions and +7.13 GHz fixed in stabilization for addressing respectively, resulting in isolated absorption resonances addressed at +57 MHz ($A_1 \rightarrow C_1$) and -69 MHz ($A_2 \rightarrow C_1$). Furthermore, one can imagine population burning by applying radio waves resonant with $B_1 \leftrightarrow A_2$ and $B_2 \leftrightarrow A_2$ to increase the population of A_1 at the address.

The use of DC magnetic fields to tune spin energy into cavity resonances is a viable option for increasing the interaction strength between spin ensemble and radio waves. However, this could further complicate the transducer application, considering the importance of isolation of field and background noises for quantum computing modules. Even if allowed, there exists strong limitations of field strength and orientation for low-loss superconducting resonators [34]. Future studies must consider the mechanical or electrical wide-tuning of resonators to achieve optimal transducer application.

Acknowledgments

This study was supported by the National Research Foundation of South Korea (NRF-2021M3E4A1038018, *Transducers between microwave and near-infrared photons based on coherent spin memory*).

- [1] R. Orbach and B. Bleaney, Proc. Math. Phys. Eng. Sci. **264**, 458 (1961).
- [2] R. Marino, Thesis, Université des Sciences et Technologie de Lille - Lille I (2011).
- [3] M. Afzelius, C. Simon, H. d. Riedmatten, and N. Gisin, Phys. Rev. A **79**, 052329 (2009).
- [4] M. Afzelius, N. Gisin, and H. d. Riedmatten, Phys. Today **68**, 42 (2015).
- [5] M. Zhong, M. P. Hedges, R. L. Ahlefeldt, J. G. Bartholomew, S. E. Beavan, S. M. Wittig, J. J. Longdell, and M. J. Sellars, Nature **517**, 177 (2015).
- [6] L. A. Williamson, Y.-H. Chen, and J. J. Longdell, Phys. Rev. Lett. **113**, 203601 (2014).
- [7] J. R. Everts, M. C. Berrington, R. L. Ahlefeldt, and J. J. Longdell, Phys. Rev. A **99**, 063830 (2019).
- [8] T. Böttger, C. W. Thiel, Y. Sun, and R. L. Cone, Phys. Rev. B **73**, 075101 (2006).
- [9] S. Blum, C. O'Brien, N. Lauk, P. Bushev, M. Fleischhauer, and G. Morigi, Physical Review A **91**, 033834 (2015).
- [10] S. Probst, H. Rotzinger, A. V. Ustinov, and P. A. Bushev, Phys. Rev. B **92**, 014421 (2015).
- [11] G. Wolfowicz, H. Maier-Flaig, R. Marino, A. Ferrier, H. Vezin, J. J. L. Morton, and P. Goldner, Phys. Rev. Lett. **114**, 170503 (2015).
- [12] P. Jobez, C. Laplane, N. Timoney, N. Gisin, A. Ferrier, P. Goldner, and M. Afzelius, Phys. Rev. Lett. **114**, 230502 (2015).
- [13] N. C. Wong, E. S. Kintzer, J. Mlynek, R. G. DeVoe, and R. G. Brewer, Phys. Rev. B **28**, 4993 (1983).
- [14] K. Holliday, X.-F. He, P. T. H. Fisk, and N. B. Manson, Opt. Lett. **15**, 983 (1990).
- [15] J. G. Bartholomew, J. Rochman, T. Xie, J. M. Kindem, A. Ruskuc, I. Craiciu, M. Lei, and A. Faraon, Nat. Commun **11**, 3266 (2020).
- [16] T. Zhong, J. M. Kindem, J. G. Bartholomew, J. Rochman, I. Craiciu, E. Miyazono, M. Bettinelli, E. Cavalli, V. Verma, S. W. Nam, et al., Science **357**, 1392 (2017).

- [17] X. Fernandez-Gonzalvo, S. P. Horvath, Y.-H. Chen, and J. J. Longdell, *Phys. Rev. A* **100**, 033807 (2019).
- [18] A. Tkalčec, S. Probst, D. Rieger, H. Rotzinger, S. Wünsch, N. Kukharchyk, A. D. Wieck, M. Siegel, A. V. Ustinov, and P. Bushev, *Phys. Rev. B* **90**, 075112 (2014).
- [19] E. A. Goldschmidt, S. V. Polyakov, S. E. Beavan, J. Fan, and A. L. Migdall, in *Conference on Lasers and Electro-Optics (CLEO)* (Optica Publishing Group, 2010), OSA Technical Digest (CD), p. QThA3.
- [20] M. Nilsson, L. Rippe, S. Kröll, R. Klieber, and D. Suter, *Phys. Rev. B* **70**, 214116 (2004).
- [21] B. Lauritzen, N. Timoney, N. Gisin, M. Afzelius, H. D. Riedmatten, Y. Sun, R. M. Macfarlane, and R. L. Cone, *Phys. Rev. B* **85**, 115111 (2012).
- [22] S. Welinski, A. Tiranov, M. Businger, A. Ferrier, M. Afzelius, and P. Goldner, *Phys. Rev. X* **10**, 031060 (2020).
- [23] S. Welinski, A. Ferrier, M. Afzelius, and P. Goldner, *Phys. Rev. B* **94**, 155116 (2016).
- [24] A. Ortu, A. Tiranov, S. Welinski, F. Fröwis, N. Gisin, A. Ferrier, P. Goldner, and M. Afzelius, *Nat. Mater* **17**, 671 (2018).
- [25] I. Usmani, C. Clausen, F. Bussi eres, N. Sangouard, M. Afzelius, and N. Gisin, *Nat. Photon.* **6**, 234 (2012).
- [26] F. Bussi eres, C. Clausen, A. Tiranov, B. Korzh, V. B. Verma, S. W. Nam, F. Marsili, A. Ferrier, P. Goldner, H. Herrmann, et al., *Nat. Photon.* **8**, 775 (2014).
- [27] A. Kiel and W. B. Mims, *Phys. Rev.* **161**, 386 (1967).
- [28] H.-J. Lim, S. Welinski, A. Ferrier, P. Goldner, and J. J. L. Morton, *Phys. Rev. B* **97**, 064409 (2018).
- [29] J. D. Pritchard, J. A. Isaacs, M. A. Beck, R. McDermott, and M. Saffman, *Phys. Rev. A* **89**, 010301 (2014).
- [30] J. I. Thorpe, K. Numata, and J. Livas, *Opt. Express* **16**, 15980 (2008).
- [31] Z. Fang, H. Cai, G. Chen, and R. Qu, *Optical Phase Locked Loop and Frequency Transfer* (Springer Singapore, Singapore, 2017), pp. 235–266.
- [32] J. M. Kindem, J. G. Bartholomew, P. J. T. Woodburn, T. Zhong, I. Craiciu, R. L. Cone, C. W. Thiel, and A. Faraon, *Phys. Rev. B* **98**, 024404 (2018).
- [33] M. D. Levenson and S. S. Kano, in *Introduction to Nonlinear Laser Spectroscopy (Second Edition)* (Academic Press, 1988), pp. 29–77, second edition ed.

[34] C. Song, Physics - dissertations. 118., Syracuse University (2011).

Supplementary Materials

S6. DETAILS OF THE PUMP-PROBE SPECTROSCOPY RESULTS

We fitted each resonance signal in the pump-probe saturation spectrum (Fig. 3) into a line-shape model of the frequency-demodulated signal of a Lorentzian spectral response:

$$I(\omega) = \text{Re} [F^*(\omega - \omega_0)F(\omega - \omega_0 + \nu) - F(\omega - \omega_0)F^*(\omega - \omega_0 - \nu)], \quad (3)$$

where $F(\omega) = (\omega + \gamma\sqrt{-1})^{-1}$ with a linewidth factor γ , phase-modulation frequency ν , and central frequency ω_0 , according to the frequency-modulation spectroscopy [33]. The values in the *frequency* and *linewidth* columns display the parameters of ω_0 and half-width-half-maximum linewidth converted from γ , respectively. Values in the frequency and linewidth columns are resulted parameters of a center position and a half-width-half-maximum linewidth. Numbers after the \pm sign represent 95 % confidence intervals. The *Notes* column displays the algebraic relations of frequencies and energy splittings.

The outcome of algebraic relation and the center frequency can differ within the average linewidth owing to inhomogeneous broadening. As the observed probe resonances of both the positive side and the negative side were excited by the same optical frequency for the pump laser (306.2685 THz), they originated from the $^{171}\text{Yb}^{3+}$ dopant groups of opposite resonance shifts in terms of optical inhomogeneous broadening. Considering that both optical and spin inhomogeneous broadening are caused by a mechanical strain in the Y_2SiO_5 , the probe resonances of positive and negative frequencies are seeing the reversely biased inhomogeneous broadening groups.

TABLE S1: Resonance frequencies shown in the pump-probe saturation spectrum of Figure 3

Index	Frequency (MHz)	Linewidth (MHz)	Amplitude (a.u.)	Notes	Pump	Probe
<i>f</i>	287.76 ± 0.07	0.96 ± 0.08	0.36 ± 0.01	$C_3 \rightarrow C_4$	$x \leftrightarrow C_3$	$x \leftrightarrow C_4$
<i>f</i>	-287.80 ± 0.08	1.11 ± 0.11	0.45 ± 0.01	$C_4 \rightarrow C_3$	$x \leftrightarrow C_4$	$x \leftrightarrow C_3$
<i>k</i>	-366.58 ± 0.10	1.39 ± 0.13	0.42 ± 0.01	$f(C_3 \rightarrow C_4)-f(A_1 \rightarrow A_2)$	$A_1 \leftrightarrow C_3$	$A_2 \leftrightarrow C_4$
<i>k</i>	366.72 ± 0.08	1.07 ± 0.09	0.40 ± 0.01	$f(C_4 \rightarrow C_3)-f(A_2 \rightarrow A_1)$	$A_2 \leftrightarrow C_4$	$A_1 \leftrightarrow C_3$
<i>m</i>	-415.53 ± 0.17	1.15 ± 0.27	0.25 ± 0.01	$f(A_2 \rightarrow B_2)-f(C_4 \rightarrow C_2)$	$A_2 \leftrightarrow C_4$	$B_2 \leftrightarrow C_2$
<i>a</i>	528.83 ± 0.10	1.41 ± 0.10	0.56 ± 0.01	$B_1 \rightarrow B_2$	$B_2 \leftrightarrow y$	$B_1 \leftrightarrow y$
<i>a</i>	-529.19 ± 0.09	1.37 ± 0.11	0.76 ± 0.01	$B_2 \rightarrow B_1$	$B_1 \leftrightarrow y$	$B_2 \leftrightarrow y$
	-578.18 ± 0.27	1.21 ± 0.34	0.32 ± 0.02	$f(C_2 \rightarrow C_3)-f(B_1 \rightarrow A_1)$	$B_1 \leftrightarrow C_2$	$A_1 \leftrightarrow C_3$
<i>b</i>	-654.57 ± 0.08	1.12 ± 0.10	0.70 ± 0.01	$A_1 \rightarrow A_2$	$A_1 \leftrightarrow y$	$A_2 \leftrightarrow y$
<i>b</i>	654.68 ± 0.09	0.94 ± 0.09	0.62 ± 0.01	$A_2 \rightarrow A_1$	$A_2 \leftrightarrow y$	$A_1 \leftrightarrow y$
<i>s</i>	-1136.80 ± 0.10	1.08 ± 0.12	0.27 ± 0.01	$f(C_3 \rightarrow C_2)-f(A_2 \rightarrow A_1)$	$A_2 \leftrightarrow C_3$	$A_1 \leftrightarrow C_2$
	-1184.31 ± 0.24	1.03 ± 0.35	0.15 ± 0.01	$f(A_2 \rightarrow A_1)+f(B_2 \rightarrow B_1)$		
	-1260.30 ± 0.28	1.04 ± 0.50	0.15 ± 0.02	$f(C_3 \rightarrow C_2)-f(B_2 \rightarrow B_1)$	$B_2 \leftrightarrow C_3$	$B_1 \leftrightarrow C_2$
	-1310.91 ± 0.43	1.02 ± 0.58	0.12 ± 0.02	$f(A_1 \rightarrow B_2)-f(B_2 \rightarrow B_1)$		
<i>o</i>	-1424.87 ± 0.09	1.42 ± 0.11	0.40 ± 0.01	$f(C_4 \rightarrow C_2)-f(A_2 \rightarrow A_1)$	$A_2 \leftrightarrow C_4$	$A_1 \leftrightarrow C_2$
	-1515.90 ± 0.18	1.01 ± 0.32	0.11 ± 0.01	$f(C_3 \rightarrow C_2)-f(C_4 \rightarrow C_3)$		
<i>g</i>	-1791.80 ± 0.09	1.42 ± 0.11	0.52 ± 0.01	$C_3 \rightarrow C_2$	$x \leftrightarrow C_3$	$x \leftrightarrow C_2$
<i>c</i>	-1841.27 ± 0.07	1.43 ± 0.10	0.54 ± 0.01	$A_1 \rightarrow B_2$	$B_2 \leftrightarrow y$	$A_1 \leftrightarrow y$
<i>h</i>	-2080.14 ± 0.07	1.15 ± 0.10	0.45 ± 0.02	$C_4 \rightarrow C_2$	$x \leftrightarrow C_4$	$x \leftrightarrow C_2$
<i>p</i>	-2094.14 ± 0.09	1.29 ± 0.10	0.79 ± 0.01	$f(C_2 \rightarrow C_1)-f(B_2 \rightarrow B_1)$	$B_2 \leftrightarrow C_2$	$B_1 \leftrightarrow C_1$
<i>d</i>	-2370.58 ± 0.09	1.22 ± 0.10	0.45 ± 0.01	$A_1 \rightarrow B_1$	$B_1 \leftrightarrow y$	$A_1 \leftrightarrow y$
<i>q</i>	-2445.74 ± 0.35	1.17 ± 0.39	0.20 ± 0.01	$f(C_3 \rightarrow C_2)-f(A_1 \rightarrow A_2)$	$A_1 \leftrightarrow C_3$	$A_2 \leftrightarrow C_2$
<i>e</i>	-2496.13 ± 0.11	1.56 ± 0.13	0.35 ± 0.01	$A_2 \rightarrow B_2$	$B_2 \leftrightarrow y$	$A_2 \leftrightarrow y$
<i>j</i>	-2623.10 ± 0.09	1.03 ± 0.09	0.84 ± 0.01	$C_2 \rightarrow C_1$	$x \leftrightarrow C_2$	$x \leftrightarrow C_1$

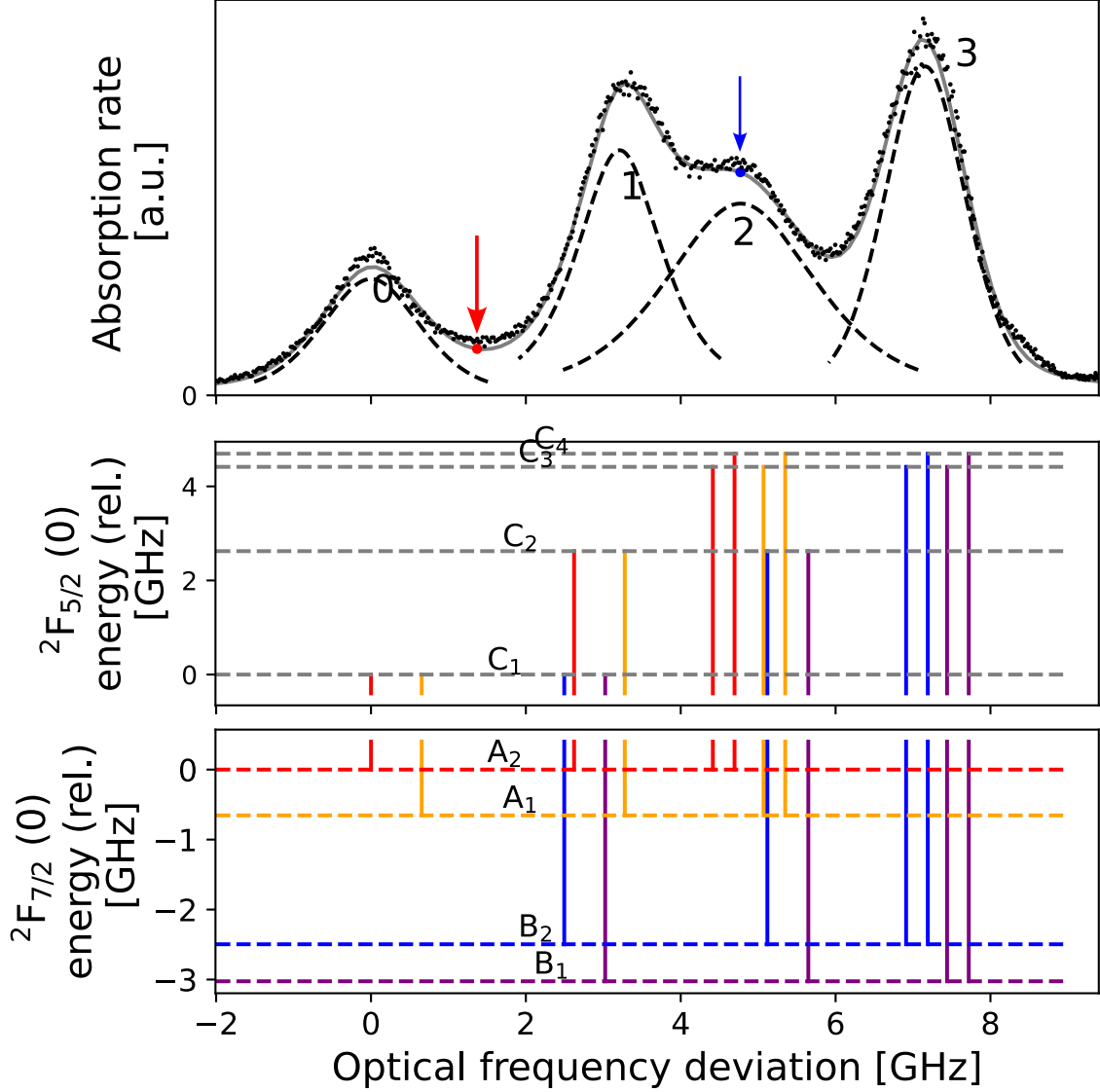


FIG. S1: (Color online) Optical absorption spectrum of $^{171}\text{Yb}^{3+}:\text{Y}_2\text{SiO}_5$ site II. The absorptions were measured for the pump laser. The horizontal axis represents optical frequency relative to 306.264 THz. Each vertical line in the energy diagrams represents a transition between $^2F_{7/2}(0)$ and $^2F_{5/2}(0)$ excitable by the optical frequency of its location.

S7. OPTICAL ABSORPTION SPECTRUM

The optical absorption spectrum of $^{171}\text{Yb}^{3+}:\text{Y}_2\text{SiO}_5$ site II was measured for optical frequencies from 306.264 THz (978.87 nm in wavelength) to +8 GHz of relative frequency. The optical frequencies were obtained from a wavelength meter with a 200 MHz accuracy. Because of optical inhomogeneous broadening between $^2F_{7/2}(0)$ and $^2F_{5/2}(0)$, 16 transitions

appeared to be 4 broad distributions (0 to 3), and their linewidths are 1.4 (0), 1.2 (1), 2.2 (2), and 1.2 GHz (3) respectively as shown as in Figure S1. Comparing the optical transition energy and the absorption spectrum, B_1 and B_2 seems to have a low absorption strength for $B_2 \rightarrow C_1$ and a preference of $\{C_2, C_3, C_3\}$ for optical excitations.

The red arrow indicates an optical frequency used for the optical Raman heterodyne measurement to detect the radio-wave resonance of the $A_1 \leftrightarrow A_2$ transition, and the blue arrow used for the pump laser in the pump-probe saturation spectroscopy.